

1 **Modelling 3D permeability distribution in alluvial fans using facies architecture and** 2 **geophysical acquisitions**

3 Lin Zhu ¹, Huili Gong ¹, Zhenxue Dai ^{2,3}, Gaoxuan Guo ⁴, Pietro Teatini ⁵

4 ¹College of Resource Environment and Tourism, Capital Normal University, Laboratory Cultivation Base
5 of Environment Process and Digital Simulation, Beijing, China

6 ²Earth and Environmental Sciences Division, Los Alamos National Laboratory, Los Alamos, New
7 Mexico, United States

8 ³College of Construction Engineering, Jilin University, Changchun, 130021, China

9 ⁴Beijing Institute of Hydrogeology and Engineering Geology, Beijing, China

10 ⁵Department of Civil, Environmental and Architectural Engineering, University of Padova, Italy

11 *Correspondence to:* Lin Zhu hi-zhulin@163.com; Huili Gong gonghl@263.com

12

13 **Abstract.** Alluvial fans are highly heterogeneous in hydraulic properties due to complex depositional
14 processes, which make it difficult to characterize the spatial distribution of the hydraulic conductivity (K).
15 An original methodology is developed to identify the spatial statistical parameters (mean, variance,
16 correlation range) of the hydraulic conductivity in a three-dimensional setting by using geological and
17 geophysical data. More specifically, a large number of inexpensive vertical electric soundings is
18 integrated with a facies model developed from borehole lithologic data to simulate the $\log_{10}(K)$ continuous
19 distributions in multiple-zone heterogeneous alluvial megafans. The Chaobai River alluvial fan in the
20 Beijing Plain, China, is used as an example to test the proposed approach. Due to the non-stationary
21 property of the K distribution in the alluvial fan, a multi-zone parameterization approach is applied to
22 analyze the conductivity statistical properties of different hydrofacies in the various zones. The composite
23 variance in each zone is computed to describe the evolution of the conductivity along the flow direction.
24 Consistently with the scales of the sedimentary transport energy, the results show that conductivity
25 variances of fine sand, medium-coarse sand, and gravel decrease from the upper (Zone 1) to the lower
26 (Zone 3) portion along the flow direction. In Zone 1, sediments were moved by higher-energy flooding,
27 which induces poor sorting and larger conductivity variances. The composite variance confirms this
28 feature with statistically different facies from Zone 1 to Zone 3. The results of this study provide insights

29 to improve our understanding on conductivity heterogeneity and a method for characterizing the spatial
30 distribution of K in alluvial fans.

31

32

33 **1 Introduction**

34 Alluvial fans usually house valuable groundwater resources because of significant water storage and
35 favorable recharge conditions. Sedimentary processes forming alluvial fans are responsible for their
36 complex long-term evolution. Usually, the coarsest material (gravel) is deposited in the upper fan, with
37 the gravel passing into sand in the middle of the fan and then into silt and clay in the tail. A high
38 heterogeneity characterizes the deposit distribution because of the shifting over time of the sediment-
39 transporting streams (Zappa et al., 2006; Weissmann et al., 1999).

40 Hydraulic conductivity distributions in alluvial fans can be assigned according to the various hydrofacies
41 simulated by conditional indicator geostatistical methods (Eggleston and Rojstaczer 1998; Fogg et al.,
42 1998; Weissmann and Fogg, 1999; Weissmann et al., 2002a, 2002b; Ritzi et al., 2004, 2006; Proce et al.,
43 2004; Dai et al., 2005; Harp et al., 2008; Hinnell et al., 2010; Maghrebi et al., 2015; Soltanian et al., 2015;
44 Zhu et al., 2015a). However, the geostatistical methods require the stationary assumption, i.e. the
45 distribution of the volumetric proportions and correlation lengths of hydrofacies converge to their mean
46 values in the simulation domain. The hydrofacies and hydraulic conductivity (K) distributions in alluvial
47 fans are generally non-stationary (Weissmann et al., 1999; Anderson, 2007; Weissmann et al., 2010, 2013;
48 Zhu et al., 2016a). Hence, the use of these methods may cause large characterization errors and add
49 significant uncertainty to the predictions achieved by groundwater flow and contaminant transport models

50 (Eggleston and Rojstaczer 1998; Irving and Singha 2010; Dai et al., 2014a). Zhu et al., (2016a) adopted
51 a local-stationary assumption by dividing the alluvial fan into three zones along the flow direction of the
52 Chaobai River, China. The zones were properly detected based on the statistical facies distribution. Then,
53 the indicator simulation method was applied to each zone and the simulated hydrofacies distribution in
54 the three zones was used to guide modelling the K distribution.

55 Hydraulic conductivity of granular deposits generally varies with grain size, porosity, and sorting.
56 Traditional methods for K estimate, e.g. well test, permeability measurements, and grain-size analyses
57 (Niwas et al., 2011), are very expensive, time-consuming, and make difficult to provide representative
58 and sufficient field data for addressing spatial variations of conductivity. Recently, data fusion techniques
59 have been developed for coupled inversion of multi-source data to estimate K distributions for
60 groundwater numerical modeling. Geophysical data (such as surface electric resistivity and various
61 logging data) are relatively inexpensive and can provide considerable information for characterizing
62 subsurface heterogeneous properties (Hubbard et al., 2001; Yeh et al., 2002; Dai et al., 2004a; Morin
63 2006; Sikandar et al., 2010; Bevington et al., 2016). Electric resistivity data have been proven useful to
64 derive sediment porosity distributions (Niwas and Singhal 1985; Niwas et al., 2011; Niwas and Celik
65 2012; Zhu et al., 2016b). Zhu et al. (2016b) simulated the spatial distributions of hydraulic conductivity
66 by combing the interpolated resistivity on basis of VES and the stochastic simulated facies through
67 empirical equation, in which the hydraulic conductivity was converted from the porosity data calculated
68 from resistivity measurements and the grain size.

69 This study proposes a novel approach to reconstruct the three-dimensional configuration of conductivity
70 in alluvial fans by combining the hydrofacies spatial heterogeneity provided by a multi-zone transition

71 probability model with hydrogeological and hydrogeophysical measurements, in particular inexpensive
72 vertical electrical soundings (VES) properly calibrated through resistivity logs acquired in a few
73 wellbores. We assume the K distributions are local-stationary, i.e. the mean and variance of log
74 conductivity are convergent in each hydrofacies and in each local zone. Therefore, we can compute the
75 $\log_{10}(K)$ semivariogram in each hydrofacies and in each zone. The spatial structure features of hydraulic
76 conductivity deduced from semivariograms are used during the geostatistical simulation processes of the
77 hydraulic conductivity. The Chaobai alluvial fan (or called “megafan” as defined by Leier et al. (2005)
78 and Hartley et al. (2010) for very large alluvial fans) in the northern Beijing Plain, China, was selected as
79 study area to test the proposed integrated approach.

80

81 **2 Material and Methods**

82 **2.1 Study area**

83 The study area belongs to the Chaobai River alluvial fan (or megafan), in the northern Beijing Plain
84 (northern latitude 40° - $40^{\circ}30'$, eastern longitude $116^{\circ}30'$ - 117°), with an area of $1,150 \text{ km}^2$ (Fig. 1a). The
85 Chaobai River is the second largest river flowing through the Beijing Plain from north to south. The
86 ground elevation decreases southward with an average 2‰ slope. Quaternary sediments were mainly
87 deposited by flooding events with turbulent flow and consist of porous strata containing groundwater.
88 The aquifer system in the alluvial fan can be divided into three zones according to the lithological features
89 (Fig. 1): an upper fan zone (or Zone 1) with coarse sediments (e.g., sandy-gravel aquifers), a middle upper
90 fan zone (or Zone 2) where medium-coarse sediments (e.g., sandy-gravel to sandy-silt aquifers) were

91 deposited , and a fine-sediment (e.g., sand and clay multiple aquifers) middle-lower fan zone (or Zone 3).
92 Four hydrofacies, including sub-clay and clay (C), fine sand (FS), medium-coarse sand (MS), and gravel
93 (G), were classified based on the interpretations of the cores and textural description of almost 700
94 boreholes (Zhu et al., 2015).

95 The study area is one of the most important regions for the supply of groundwater resource to Beijing.
96 The Huairou emergency groundwater resource region (hereafter EGRR) with an area of 54 Km² is located
97 in Zone 1. The total groundwater withdrawal amounted to 1.2×10^8 m³ in 2003. Several well-fields
98 belonging to the so-called "water supply factory" were drilled along the Chaobai River in Zone 1 and the
99 upper Zone 2. Most of these well-fields were built in 1979 with a designed groundwater pumping volume
100 of 1.6×10^8 m³ per year. The average thickness of the exploited aquifer system is approximately 300 m.
101 The long-term over-exploitation of the aquifer system has resulted in a serious drawdown of water levels,
102 which has reduced the exploitable groundwater resources and induced geological disasters, mainly land
103 subsidence, fault reactivation, and ground fissures (Cheng et al., 2015; Yang et al., 2015; Zhu et al., 2015).
104 In 2010, the annual groundwater withdrawal at the EGRR and the water factory decreased to 0.86×10^8
105 m³ and 0.65×10^8 m³, respectively.

106 The largest cumulative land subsidence from June 2003 to January 2010 was quantified in approximately
107 340 mm by Zhu et al., (2013, 2015) in Tianzhu County to the south. The characterization of the
108 distribution and spatial variability of the hydraulic conductivity is vital for an optimal use of the limited
109 water resources in this area.

110 **2.2 Methodological approach**

111 Nowadays, a large set of hydraulic conductivity samples can be derived by integrating appropriate
112 relations of various geological data, including hydrogeophysical measurements, borehole
113 lithostratigraphies, and hydrogeological information (total dissolved solid TDS and groundwater level).
114 These databases can be statistically processed to derive the spatial variation of $\log_{10}(K)$ for various facies,
115 including clay, fine sand, medium-coarse sand, and gravel.

116 In this paper, the statistical assessment is separately carried out for separated zones, building-up
117 experimental semivariograms that are fitted with exponential models. The optimal parameters of these
118 latter are estimated through a generalized output least squares (OLS) criterion. Then, the composite
119 semivariograms are computed using a hierarchical sedimentary architecture (Ritzi et al., 2004; Dai et al.,
120 2005) to obtain the K variance in each zone. Finally, the configuration of $\log_{10}(K)$ is simulated through a
121 multiple-zone sequential Gaussian algorithm with estimated statistic parameters reflecting the K spatial
122 structures in the alluvial fan. Figure 2 shows the steps involved in the developed approach.

123 **2.3 Data set**

124 **2.3.1 Geophysical data**

125 Geophysical data include resistivity loggings and vertical electrical soundings. There are six well-electric
126 logs continuously recording the formation resistivity versus depth. Five logs were collected in Zone 2 and
127 one in Zone 3. Each well log has a lithological description, which helps to relate the resistivity values to
128 the corresponding facies.

129 The average resistivity of G is the largest, with a value of $198 \Omega \text{ m}$, and that of C is the smallest with a
130 value of $24 \Omega \text{ m}$. Figure 3 compares the outcome of logging data in term of resistivity versus depth and

131 the corresponding stratigraphy, where the groundwater depth is 12 m. The log was acquired in the eastern
132 part of Zone 2. The average resistivity from 32.4 m to 40.5 m depth, where the sediments are mainly G
133 and MS, is 70.8 Ω m. The resistivity curve shows two evident peaks from 97 m to 102 m and between 81
134 m and 84.5 m depth, where the MS is located.

135 The C resistivity is relatively low due to the good intrinsic electrical conductivity of this facies. For
136 example from 16.5 m to 23.5 m depth, where C is the prevalent facies, a low resistivity equal to 27.2 Ω
137 m is recorded. Since a hydrofacies with a smaller grain size has a greater total surface area, the resistivity
138 difference can partially reflect the distributions of particle sizes and the hydrofacies composition. Since
139 the obtained resistivity is the apparent resistivity, we used the resistivity located in the middle of the facies
140 block, where the resistivity is approximate to the real resistivity. Unfortunately, it is unknown to the
141 authors if the logs were calibrated in the field and how the salinity of the formation water, although
142 minimal and almost independent on the site and depth, has been accounted for. On the other hand, the
143 resistivity distributions have good correlations with different hydrofacies along the vertical and horizontal
144 directions. Therefore, in the mathematical framework that follows, we have assumed that the logs have
145 been calibrated and are accurate enough for presenting our work as a proof of concept.

146 Vertical electrical soundings (VES) using the Schlumberger electrode configuration were carried out by
147 the Beijing Institute of Hydrogeology and Engineering Geology (BIHEG). A number of 113 detecting
148 positions were selected, with a maximum half current electrode space equal to 340 m and the potential
149 electrode space ranging from 1 to 30 m. All the sounding data (1356 VES measurements) recorded the
150 apparent resistivity of the porous medium. These data were inverted to real resistivity using the nonlinear

151 Occam inversion method (Constable et al., 1987), with a low root mean square relative error of 2%. Figure
152 4 shows the layered structure fitting model of resistivity and the borehole lithologic observations. The
153 inversed resistivity generally reflects the difference of facies: the thick gravel layer has larger resistivity
154 while the fine sand and clay layers have relatively smaller resistivity.

155 **2.3.2 Geological and hydrogeological data**

156 Almost 700 borehole lithologic logs were collected in the study area. The sedimentary deposits show large
157 heterogeneity from the upper to the lower fan zone. In Zone 1, the dominant facies is G with a volumetric
158 proportion of 53%. The volumetric proportion of C is 16%. In Zone 2, the volumetric proportion of C
159 increases to 40%, while that of G decreases sharply to 24%. In Zone 3, the proportion of G decreases
160 further to 6% and that of C increases to 50% (Table 1). More detailed information is given in Zhu et al.,
161 (2016a). The lithological information in a buffer zone of 200 m around the VES locations has been used
162 to represent the actual facies distribution in the area surrounding the sites of the geophysical acquisitions.
163 A number of 35 hydrochemistry measurements with a depth from 20 m to 270 m were obtained throughout
164 the area. The minimum, maximum and average TDS values are 423 mg/l at the depth of 180 m, 943 mg/l
165 at the depth of 50 m, and 692 mg/l, respectively. Generally, the TDS is very low with the higher values
166 measured in the south-western part of the study area. Because of the relatively small dataset and the
167 observed low variability, in this paper the TDS variation in the vertical direction has been neglected. A
168 TDS map was obtained by interpolating the available records using an Ordinary Kriging method with a
169 spherical semivariogram model.

170 A large number of depth of water level measurements were also collected to map the thickness of the
171 unsaturated unit. The TDS and groundwater level at each VES and resistivity log location were derived
172 from the interpolated surfaces.

173 **2.3.3 Hydraulic conductivity estimates from geophysical acquisitions**

174 The hydraulic conductivity K was estimated using the Kozeny-Carman equation:

$$175 \quad K(x, y, z) = \frac{\delta g}{\mu} \times \frac{d_{(x,y,z)}^2}{180} \frac{\phi_{(x,y,z)}^3}{(1-\phi_{(x,y,z)})^2} \quad (1)$$

176 which is widely accepted to derive the hydraulic conductivity from grain size and porosity (Soupios et
177 al., 2007; Utom et al., 2013; Khalil et al., 2013; Zhu et al., 2016). In Eq. (1), $d_{(x,y,z)}$ is the median grain
178 diameter (D50, mm) at location (x,y,z) , which was determined according to the lithology information (or
179 lithological descriptions and grain size distributions), g is gravity, μ the kinematic viscosity (kg/(m·s)), δ
180 the fluid density, and $\phi_{(x,y,z)}$ the porosity. ϕ was estimated using Archie's law (Eq. (2)), which relates the
181 bulk resistivity of granular medium to porosity:

$$182 \quad \rho = \alpha \rho_w \phi^{-m} S_w^{-n} \quad (2)$$

183 where ρ is the saturated formation resistivity (Ω m), α the pore-geometry coefficient associated with the
184 medium ($0.5 \leq \alpha \leq 2.5$), m the cementation factor ($1.3 \leq m \leq 2.5$) (Massoud et al., 2010; Khalil and Santos
185 2013). α is set as 1. In the upper part of alluvial (Zone 1 and Zone 2) m is set as 1.3 due to the sand is
186 unconsolidated. In Zone 3 m is set as 1.7 which reflects slightly cemented sandstones (Niwas et al. 2011).
187 s_w the water saturation, and n the saturation index. The pore fluid resistivity (Ω m) ρ_w is calculated using
188 the following experimental relation:

189

$$\rho_w = \frac{5.6(\text{TDS})^b}{1+\beta(t-18)} \quad (3)$$

190 with TDS in (g/L), temperature t in ($^{\circ}\text{C}$), b and β being constant parameters (Wu et al., 2003). For the
191 most common electrolytes, $b = -0.95$ and $\beta = 0.025$. Note that the parameters associated with equations
192 (2) and (3) are site specific and application these equations to other sites will need re-adjust the related
193 parameters.

194 The logarithmically transformed values of the estimated hydraulic conductivity ($\log_{10}(K)$) were used for
195 the geostatistical analysis because of its normal distribution (Neuman, 1990). The histograms of $\log_{10}(K)$
196 values within each facies are in Fig. 5. There are 102, 2077, and 1716 conductivity samples in Zone 1,
197 Zone 2, and Zone 3, respectively. Considering that Archie's law can only be used for clay-free granular
198 sediments, the K values of C were not estimated in this study. Based on the lithological description
199 information of borehole data, it has been reasonably assumed that clay fraction is negligible in G, MS,
200 and FS facies. The statistics of $\log_{10}(K)$ for the three facies in three zones are listed in Table 2. The mean
201 $\log_{10}(K)$ values decrease from Zone 1 to Zone 3, consistently with the sedimentary transport processes in
202 the alluvial fan. In the upper region (Zone 1), high water flowing energy made the deposits consisted
203 mainly of larger-grained particles and the coarse-grained sediments are dominant. In the southern part
204 (Zone 3), the deposits change to relatively fine-grained particles. The mean $\log_{10}(K)$ of gravel is greater
205 than 2.4 ($\log(\text{m/d})$) and that of fine sand is less than 0.2 ($\log(\text{m/d})$). The lithological information at the
206 depth of the conductivity samples shows that volumetric proportions of FS and MS increase and that of
207 G decreases from Zone 1 to Zone 3. The results are consistent with the statistic outputs deduced from 694
208 borehole data by Zhu et al., (2016a).

209 2.4 Statistical Methods

210 2.4.1 Semivariogram of hydraulic conductivity

211 Semivariogram describes the degree of spatial dependence of a spatial random field or stochastic process.
212 It is a concise and unbiased characterization of the spatial structure of regionalized variables, which is
213 important in Kriging interpolations and conditional simulations. The experimental semivariogram:

$$214 \hat{r}_k(h_\varphi) = \frac{1}{2N(h)} \sum_{(o,p) \in N(h)} (Y(z_o) - Y(z_p))^2 \quad (4)$$

215 can be fitted by an exponential model (e.g., Dai et al., 2014b):

$$216 r_k(h_\varphi) = \sigma^2 \left(1 - e^{\frac{-3h}{\lambda}}\right) \quad (5)$$

217 where $\hat{r}_k(h_\varphi)$ and $r_k(h_\varphi)$ are the experimental and model semivariograms of log conductivity Y for the
218 k^{th} facies at a lag distance h along the φ direction. In this paper we calculate the semivariograms in the
219 vertical and dip directions. $N(h)$ is the number of pair measuring points z_o and z_p separated by a h lag
220 distance, σ^2 is the variance, and λ the correlation range.

221 The variance and range were optimized using the least-squares criterion, which was solved by the
222 modified Gauss-Newton-Levenberg-Marquardt method (Clifton and Neuman, 1982; Dai et al., 2012).

223 The sensitivity equation method was derived to compute the Jacobian matrix for iteratively solving the
224 gradient-based optimization problem (Samper and Neuman 1986; Carrera and Neuman 1986; Dai and
225 Samper, 2004; Samper et al., 2006; Yang et al., 2014; Zhu et al., 2016a). The two sensitivity coefficients

226 $\frac{\partial r_k}{\partial \sigma^2}$ and $\frac{\partial r_k}{\partial \lambda}$ are the partial derivatives of the semivariogram with respect to variance and range:

$$227 \frac{\partial r_k}{\partial \sigma^2} = 1 - e^{\frac{-3h}{\lambda}} \quad (6)$$

228
$$\frac{\partial r_k}{\partial \lambda} = -\sigma^2 \cdot 3h \cdot e^{-\frac{3h}{\lambda}} \cdot \lambda^{-2} \quad (7)$$

229

230 **2.4.2 Composite semivariogram of log conductivity**

231 Once the facies semivariograms were obtained in each zone, the composite semivariogram $\gamma(h)$ could be
 232 calculated through the following equation (e.g., Ritzi et al., 2004):

233
$$\gamma(h_\varphi) = \sum_{k=1}^M \sum_{i=1}^M r_{ki}(h_\varphi) p_k t_{ki}(h_\varphi) \quad (8)$$

234 where p_k and $t_{ki}(h_\varphi)$ are the volumetric proportion of facies k and the transition probability from facies
 235 k to facies i in the φ direction with a h lag distance, respectively. Equation 8 delineates the composite
 236 semivarigoram with respect to the individual facies semivariogram and transition probability. The general
 237 shape function and range of the composite semivarigoram can be obtained from individual facies mean
 238 length and volumetric proportion with the methods described in Dai et al., (2005).

239 The transition probability $t_{ki}(h_\varphi)$ has an analytical solution as derived by Dai et al., (2007):

240
$$t_{ki}(h_\varphi) = p_k + (\delta_{ki} - p_k) \cdot \exp\left(-\frac{h_\varphi}{\lambda_\varphi}\right) \quad (9)$$

241 where δ_{ki} is the Kronecker delta and λ_φ is the integral scale in the direction of φ . A geostatistical modeling
 242 tool GEOST (Dai et al., 2014b) modified from the Geostatistical Software Library (Deutsch and Journel,
 243 1992) and TPROGS (Carle and Fogg, 1997) was employed to compute the sample transition probabilities
 244 in each zone. The parameters p_k and λ_φ were optimally estimated through a modified Gauss-Newton-
 245 Levenberg-Marquardt method. More details are provided by Zhu et al., (2016a). The composite
 246 semivariograms for different zones can help us to understand the heterogeneity variations from the upper

247 to lower part of the alluvial fan, as well as the stationary property (local versus regional) of the facies and
248 hydraulic conductivity distributions.

249 **2.4.3 Sequential Gaussian simulation**

250 The Sequential Gaussian simulation (SGSIM) is a widely used stochastic simulation method to create
251 numerical model of continuous variables based on the Gaussian probability density function. The process
252 is assumed to be a stationary and ergodic random process (Deutsch and Journel, 1992; Dimitrakopoulos
253 and Luo, 2004). This method can preserve the variance and correlation range observed in spatial samples.
254 SGSIM provides a standardized normal continuous distribution of the simulated variable.

255 With the assumption that the log conductivity distributions are stationary within each zone, we used
256 SGSIM simulator implemented into GEOST to model the $\log_{10}(K)$ continuous configuration under a
257 multiple-zone framework. The conductivity of the FS, MS, and G facies in each zone was simulated
258 sequentially using the structure characteristics of the semivariograms.

259 Finally, the three-dimensional conductivity configuration was derived by combining the stochastic
260 simulated facies (Zhu et al., 2016a) with the SGSIM conductivity distribution and the mean $\log_{10}(K)$ of
261 the various facies in each zone (Table 2). The stochastic simulated facies was constructed through the
262 optimized volumetric proportion and mean length of facies in three directions. The mean length in vertical
263 and dip directions were calculated through 694 borehole. The mean length in strike direction was assumed
264 as half as that in dip direction. During the facies simulation process, borehole data were used as
265 conditional data (Zhu et al., 2016a). In detail, since each cell is characterized by specific facies and zone
266 indices, its conductivity was assigned using the corresponding (in relation to the facies and the zone) 3D

267 SGSIM outcome in that position. Note that The hydrofacies (e.g., C, FS, MS and G) are defined
268 qualitatively based on the sedimentary structures, borehole lithological descriptions, and grain sizes,
269 while the conductivity samples are then deduced from geophysical measurements for each facies at each
270 zone. Since the clay contents from zone 1 to zone 3 are increased due to the changes in the sediment
271 transport conditions, for the same facies we also found this trend and the overall hydraulic conductivities
272 are decreased from zone 1 to zone 3. Since sub-clay and clay are generally characterized by a low
273 hydraulic conductivity value, a uniform K value equal to 0.0001 m/d was set to all the C cells.

274 **3 Results and Discussion**

275 **3.1 Variation of $\log_{10}(K)$ for the various facies**

276 The optimized vertical correlation range and variance of the log conductivity semivariogram (Eq. 5) are
277 listed in Table 3, along with their 95% confidence intervals. The fitting between the experimental and the
278 model semivariograms is the best in Zone 2 because of the abundant samples, while the fitting in Zone 1
279 is the worst (Fig. 6). The fitting result of the semivariogram for the G facies is the worst in Zone 1. Two
280 are the reasons: the first is the high variance of the log conductivity of gravel in this zone; the other is the
281 limited number of samples (102 samples), which makes quite small the pair numbers within each lag
282 spacing. Hence, the computed semivariogram is highly uncertain.

283 The variance of FS, MS, and G in the vertical direction decreases from Zone 1 to Zone 3. In the upper
284 alluvial fan, sediments were deposited under multiple water flowing events and with poor sorting. The
285 deposits consist of wide ranges of sediment categories and grain sizes. The variance of G is larger than
286 1.5, which reflects the high heterogeneity of hydraulic conductivity in coarse deposits. The variances of

287 FS and MS are smaller with values equal to 0.23 and 0.32, respectively. In Zone 3, these values decrease
288 to 0.05 and 0.13, respectively, with that of G sharply decreasing to 0.62. In the middle-lower fan zone,
289 the conductivity variation within each facies reduces gradually because the ground surface slope becomes
290 smaller or flat, the sediment transport energy decreases, and the deposits within the three facies are well
291 sorted.

292 Note that the ranges are correlated with the facies structure parameters such as the indicator correlation
293 scale, mean thickness (or length), and volumetric proportion (Dai et al., 2004b; 2007). The estimated
294 correlation ranges of FS, MS and G along the vertical direction in Zone 1 do not show big difference with
295 values equal to 6.0 m, 8.0 m and 6.5 m, respectively. Zone 2 was extended from the fan apex zone (Zone
296 1) with much larger area, which allows for greater preservation potential of finer sediments (such as
297 medium-coarse sand (MS), fine sand (FS), and clay or sub clay (C)) than the more proximal Zone 1.
298 Therefore, in Zone 2 the volumetric proportions for these three facies increase while that of gravel
299 decreases. The estimated ranges of G and MS are increased, respectively. In Zone 3, the range difference
300 among the three facies decreases gradually. The range of FS is about 6.0 m, which is twice as much as
301 that of MS. The spatial variation of the structure parameters of three facies causes the large changes of
302 the correlation ranges from Zone 1 to Zone 3.

303 Due to the small number of conductivity samples in Zone 1, the variance of $\log_{10}(K)$ along the dip
304 direction is calculated only in Zone 2 and Zone 3 (Table 4, Fig. 7), as observed along the vertical direction.
305 This phenomenon possibly reflects that sediment transport energy decrease along the flow direction.

306 Lower energy flow in Zone 3 cause better sediment sorting and weak heterogeneity (or lower variance)
307 in hydraulic conductivity.

308 **3.2 Compositd semivariogram of $\log_{10}(K)$**

309 The composite semivariogram in the vertical direction at each zone is calculated by Eq. (8), using the
310 volume proportions (Table 1) and transition probability (Eq. (9)) with the same values of the lag distance
311 used to compute the facies semivariograms (Fig. 8). The values of the optimized variance are 0.68, 0.11,
312 and 0.03 in Zone 1, Zone 2, and Zone 3, respectively. The high flow energy and the large number of
313 flooding events contributing to sediment deposition are the main causes of the high heterogeneity (largest
314 variance) of the deposits in the upper part of the alluvial fan. The changes of variance between the three
315 zones support the utilization of the local-stationary assumption and simulation of multiple-zone based
316 conductivity distributions for the Chaobai alluvial fan.

317 **3.3 Configuration of $\log_{10}(K)$**

318 The configuration of $\log_{10}(K)$ in three dimensions is showed in Fig.9. The distribution of conductivity is
319 generally consistent with that of the facies. Coarse units are more frequently distributed in the upper zone,
320 which makes the average K is much larger in this zone than that in the lower part of the alluvial fan. The
321 regions with high conductivity (red color in Fig. 8) in Zone 1 are more continuous than that in other parts.
322 The adjacent cells with the smallest conductivity (blue color in Fig. 8) are obviously located mainly in
323 Zone 3. The mean conductivity is smaller in the southern part of the study area, where the piezometric
324 drawdowns in the multi-layer aquifer system were larger and the surface subsidence more serious (Zhu
325 et al., 2013, 2015). Note that since we simulated the dip direction along the main water flow direction

326 and, due to the lack of enough data, the strike-directional semivariogram is assumed to be similar as that
327 in dip direction, the simulated facies in the fan apex did not show a radiating pattern. More information
328 about simulating the radiating pattern can be found from Carle et al. (1997) and Fogg et al. (1998).

329 Based on the three dimensional K configuration, the average value of K in the depth range from 0 m to
330 300 m amounts to 194 m/d, 25 m/d and 4 m/d in Zone 1, Zone 2, and Zone 3, respectively. These values
331 are comparable with those provided by the Beijing Institute of Hydrogeology and Engineering Geology
332 (2007) based on a number of pumping tests carried out over several years in the study area. In this BIHEG
333 report the average value of K is >300 m/d in Zone 1, between 30 and 100 m/d in Zone 2, and <30 m/d
334 in Zone 3 (Fig. 1b). The fact that the arithmetic average K values are gently smaller than these latter are
335 likely due to the fact that the outcome of pumping tests are generally more representative of coarser
336 sediments.

337 Investigating the stochastic results along the vertical direction, it is interesting to notice that the average
338 K in deep units of Zone 1 and Zone 2 is smaller than that in the shallow strata. For example, in Zone 1
339 the average K for the cells from 0 m to 100 m deep is 295 m/d, which is three times as much the value for
340 the depth range between 200 m and 300 m. Conversely, no significant variation of K versus depth is
341 observed in Zone 3, with only a small decrease of the average K from the deeper to the shallower units.

342 **4 Conclusions**

343 This paper proposes a geostatistical method under a multiple zone framework, properly supported by a
344 large number of geophysical investigations, to detect the distribution and the related variance of the
345 hydraulic conductivity in three-dimensional domains. In particular, the optimized statistical parameters

346 (e.g., log conductivity variance and correlation range) of semivariograms are estimated using the modified
347 Gauss-Newton-Levenberg-Marquardt method. The Chaobai alluvial fan is used as a case study area.
348 Multiple data including downhole resistivity logging data, vertical electric soundings, well-bore lithologic
349 logs, TDS measurements, and depths to the water table are integrated to derive a dataset of conductivity
350 values in a three-dimensional setting. Log conductivity semivariograms fitted with exponential functions
351 were constructed for three facies, including fine sand, medium-coarse sand and gravel, in each of the three
352 zones into which the Chaobai fan is divided to guarantee local stationarity of the statistical process. The
353 composite semivariogram of the three facies has been derived for the two zones where a sufficiently large
354 number of samples are available. The $\log_{10}(K)$ configuration is simulated using the sequential Gaussian
355 simulation model based on statistic parameters of $\log_{10}(K)$ and the structure suggested by a 3D hydrofacies
356 simulation.

357 For the specific test case, the variance along the vertical direction of fine sand, medium-coarse sand, and
358 gravel decreases from the upper part of the alluvial fan, where the values amount to 0.23, 0.32, and 1.60,
359 to the lower portion of the Chaobai plan with values of 0.05, 0.126, and 0.62, respectively. This behavior
360 reflects the higher transport energy in the upper alluvial fan that causes a poor sediment sorting. In the
361 middle alluvial fan, the transport energy decreases and the sediments tend to be relatively well-sorted.
362 The variance of the gravel is larger than that of other lithologies. The different flow energy significantly
363 affected the coarse sediments in the vertical direction. Along the dip direction, the variance of three facies
364 (gravel, medium-coarse sand and fine sand) in the middle fan is larger than that in the lower fan. The
365 composite variance of $\log_{10}(K)$ in the vertical direction shows that the large heterogeneity in the upper
366 fan (with a value of 0.68) decreases in the lower zone.

367 The distribution of hydraulic conductivity is consistent with that of the facies. Hydraulic conductivity is
368 much larger in the upper zone than that in the lower part of the alluvial fan. This result provides valuable
369 insights for understanding the spatial variations of hydraulic conductivity and setting-up groundwater
370 flow, transport, and land subsidence models in alluvial fans.

371 Concluding, it is worth highlighting that we depicted an original method to detect the variance and
372 configuration of conductivity by fusing multiple-source data in three-dimensional domains. The proposed
373 approach can be easily used to statistically characterize the hydraulic conductivity of the various alluvial
374 fans that worldwide are strongly developed to provide high-quality water resources. We are aware of
375 some restrictions in the dataset available at the date for the Chaobai alluvial fan, for example the assumed
376 uniform distribution of TDS versus depth and the relatively small number of the conductivity samples in
377 the upper fan zone. A more accurate description of the semivariograms in the dip and lateral directions will
378 be included in our future study to improve the developed three-dimensional permeability field. Moreover,
379 our assumption that the logs are well-calibrated might be another source of uncertainty that can be reduced
380 in our next-step work. Nonetheless, the proposed methodology will be re-applied in the near future as
381 soon as new information will become available, thus allowing to improve the estimation accuracy of
382 spatial statistics parameters and the configuration of hydraulic conductivity in this Quaternary system so
383 important for the Beijing water supply.

384 **Data availability**

385 The geophysical measurements, borehole lithostratigraphies, and hydrogeological information in the
386 north part of Beijing Plain can be partly accessible by contacting Beijing Institute of Hydrogeology and
387 Engineering Geology.

388 **Author contribution**

389 Lin Zhu, Huili Gong and Zhenxue Dai derived the method of spatial variance and 3D configuration of
390 conductivity, performed data analysis and wrote the draft manuscript. Gaoxuan Guo collected the
391 geological and geophysical data, discussed the results. Pietro Teatini discussed the results, reviewed and
392 revised the manuscript.

393 **Competing interests**

394 The authors declare that they have no conflict of interest.

395 **Acknowledgements**

396 This work was supported by the National Natural Science Foundation (No.41201420, 41130744) and
397 Beijing Nova Program (No.Z111106054511097). Pietro Teatini was partially supported by the University
398 of Padova, Italy, within the 2016 International Cooperation Program.

399 **References**

- 400 Anderson, M.P.: Introducing groundwater physics, *Phys. Today*, 42–47, 2007
- 401 Beijing Institute of Hydrogeology and Engineering Geology: Groundwater flow model and the potential
402 groundwater resources in Beijing Plain, Internal Report, 60-64., 2007 (In Chinese)
- 403 Bevington, J., Piragnolo, D., Teatini, P., Vellidis, G., and Morari, F.: On the spatial variability of soil
404 hydraulic properties in a Holocene coastal farmland, *Geoderma*, 262: 294-305,
405 doi:10.1016/j.geoderma.2015.08.025, 2016.

406 Carle, S.F., and Fogg, G.E.: Modeling spatial variability with one and multidimensional continuous-lag
407 Markov chain, *Math. Geol.*, 29(7): 891-918, doi: 10.1023/a:1022303706942, 1997.

408 Carrera, J., and Neuman, S.P.: Estimation of aquifer parameters under steady state and transient condition:
409 2. Uniqueness, stability, and solution algorithms, *Water Resour. Res.*, 22, 211 – 227, doi:
410 10.1029/wr022i002p00211, 1986.

411 Cheng, G., Wang, H., Luo, Y., and Guo, H.: Study of the deformation mechanism of the Gaoliying ground
412 fissure: Prevention and Mitigation of Natural and Anthropogenic Hazards due to Land Subsidence - Proc.
413 IX Int. Symp. on Land Subsidence, K. Daito et al. eds., Proc. IAHS, UK, 231-234, 2015.

414 Clifton, P.M., and Neuman, S.P.: Effects of kriging and inverse modeling on conditional simulation of
415 the Avra Valley aquifer in southern Arizona, *Water Resour. Res.*, 18, 1215-1234, doi:
416 10.1029/wr018i004p01215, 1982.

417 Constable, S.C., Parker, R.L., and Constable, C.G.: Occam's inversion: A practical algorithm for
418 generating smooth models from electromagnetic sounding data, *Geophysics*, 52, 289-300, 1987.

419 Dai, Z., and Samper, J.: Inverse problem of multicomponent reactive chemical transport in porous media:
420 Formulation and applications, *Water Resour. Res.*, 40, W07407, doi: 10.1029/2004wr003248, 2004.

421 Dai, Z., Ritzi, R., and Dominic, D.: Estimating parameters for hierarchical permeability correlation
422 models. Aquifer Characterization, Bridge, J.S. and Hyndman, D.W. *SEPM Society for Sedimentary*
423 *Geology*, USA, 41-54, doi: 10.2110/pec.04.80.0041, 2004a.

424 Dai, Z., Ritzi, R., Huang, C., Dominic, D., and Rubin, Y.: Transport in heterogeneous sediments with
425 multimodal conductivity and hierarchical organization across scales, *J. of Hydrol.*, 294, 68-86, doi:
426 10.1007/s00477-014-0922-3, 2004b.

427 Dai Z., Ritzi, R., and Dominic, D.: Improving permeability semivariograms with transition probability
428 models of hierarchical sedimentary architecture derived from outcrop analog studies. *Water Resour. Res.*,
429 14 W07032, doi: 10.1029/2004wr003515, 2005.

430 Dai, Z., Wolfsberg, A., Lu, Z., and Ritzi, R.: Representing aquifer architecture in macrodispersivity
431 models with an analytical solution of the transition probability matrix. *Geophys. Res. Lett.*, 34, L20406,
432 doi: 10.1029/2007GL031608, 2007.

433 Dai, Z., Wolfsberg, A., Reimus, P., Deng, H., Kwicklis, E., Ding, M., Ware, D., and Ye, M.: Identification
434 of sorption processes and parameters for radionuclide transport in fractured rock, *J. Hydrol.*, 414-415,
435 220-230, doi: 10.1016/j.jhydrol.2011.10.035, 2012.

436 Dai, Z., Stauffer, P. H., Carey, J. W., Middleton, R. S., Lu, Z., Jacobs, J. F., Hnottavange-Telleen, K. &
437 Spangle, L. Pre-site characterization risk analysis for commercial-scale carbon sequestration. *Environ.*
438 *Sci. Technol.* 48, 3908–3915, 2014a.

439 Dai, Z., Middleton, R., Viswanathan, H., Fessenden-Rahn, J., Bauman, J., Pawar, R., Lee, S., and
440 McPherson, B.: An integrated framework for optimizing CO₂ sequestration and enhanced oil recovery.
441 *Environ. Sci. Technol. Lett.*, 1, 49-54, doi: 10.1021/ez4001033, 2014b.

442 Deutsch, C.V., and Journel, A.G. GSLIB: Geostatistical software library, Oxford Univ. Press. New York,
443 340, 1992.

444 Dimitrakopoulos, R., and Luo, X.: Generalized sequential Gaussian simulation on group size v and
445 screen-effect approximations of large field simulations. *Math. Geol.*, 36, 567-590, doi:
446 10.1023/b:matg.0000037737.11615.df, 2004.

447 Eggleston, J., and Rojstaczer, S.: Identification of large-scale hydraulic conductivity trends and the
448 influence of trends on contaminant transport. *Water Resour. Res.*, 34, 2155-2186, doi:
449 10.1029/98wr01475, 1998.

450 Fogg, G.E., Noyes, C.D., and Carle, S.F.: Geologically based model of heterogeneous hydraulic
451 conductivity in an alluvial setting, *Hydrogeol. J.*, 6(1), 131-143, doi: 10.1007/s100400050139, 1998.

452 Harp, D., Dai, Z., Wolfsberg, A., and Vrugt, J.: Aquifer structure identification using stochastic inversion,
453 *Geophys. Res. Lett.*, 35, L08404, doi: 10.1029/2008gl033585, 2008.

454 Hartley, A.J., Weissmann, G.S., Nichols, G.J., and Warwick, G.L., Distributive fluvial systems:
455 characteristics, distribution, and controls on development, *J. of Sediment. Res.*, 79, 167-183, doi:
456 10.2110/jsr.2010.016, 2010.

457 Hinnell, A.C., Ferre, T.P.A., Vrugt, J., Huisman, J.A., Moysey, S., Rings, J., and Kowalsky, M.B.:
458 Improved extraction of hydrologic information from geophysical data through coupled hydrogeophysical
459 inversion. *Water Resour. Res.*, 46, doi: 10.1029/2008wr007060, 2010.

460 Hubbard, S.S., Chen, J.S., Peterson, J., Majer, E.L., Williams, K.H., Swift, D.J., Mailloux, B., and Rubin,
461 Y.: Hydrogeological characterization of the South Oyster Bacterial Transport site using geophysical data,
462 *Water Resour. Res.*, 37, 2431-2456, doi: 10.1029/2001wr000279, 2001.

463 Irving, J., and Singha, K.: Stochastic inversion of tracer test and electrical geophysical data to
464 estimate hydraulic conductivities, *Water Resour. Res.*, 46, W11514, doi: 10.1029/2009WR008340, 2010.

465 Khalil, M.A., and Santos, F.A.M.: Hydraulic conductivity estimation from resistivity logs: a case study
466 in Nubian sandstone aquifer. *Arab. J. Geosci.*, 6, 205-212. doi: 10.1007/s12517-011-0343-2, 2013.

467 Leier, A.L., P. G. DeCelles, J. D. Pelletier, Mountains, monsoons, and megafans, *Geology*, 33, 289-292.
468 doi: 10.1130/G21228.1, 2005.

469 Maghrebi, M., Jankovic, I., Weissmann, G.S., Matott, L.S., Allen-King, R.M., and Rabideau, A.J.,
470 Contaminant tailing in highly heterogeneous porous formations: Sensitivity on model selection and
471 material properties. *J. of Hydrol.*, 531, 149-160. doi: 10.1016/j.jhydrol.2015.07.015, 2015.

472 Massoud, U., Santos, F.A.M., Khalil, M. A., Taha, A., and Abbas, A. M.: Estimation of aquifer hydraulic
473 parameters from surface geophysical measurements: a case study of the Upper Cretaceous aquifer, central
474 Sinai, Egypt, *Hydrogeol. J.*, 18, 699-710, doi: 10.1007/s10040-009-0551-y, 2010.

475 Morin, R.H.: Negative correlation between porosity and hydraulic conductivity in sand-and-gravel
476 aquifers at Cape Cod, Massachusetts, USA, *J. Hydrol.*, 316, 43-52, doi:10.1016/j.jhydrol.2005.04.013,
477 2006.

478 Neuman, S.P.: Universal scaling of hydraulic conductivities and dispersivities in geologic media, *Water*
479 *Resour. Res.*, 26, 1749-1758, 1990.

480 Niwas, S., and Singhal, D.C.: Aquifer transmissivity of porous media from resistivity data, *J. Hydrol.*, 82,
481 143-153, doi: 10.1016/0022-1694(85)90050-2, 1985.

482 Niwas, S., Tezkan, B., and Israil, M.: Aquifer hydraulic conductivity estimation from surface
483 geoelectrical measurements for Krauthausen test site, Germany, *Hydrogeol. J.*, 19, 307-315, doi:
484 10.1007/s10040-010-0689-7, 2011.

485 Niwas, S., and Celik, M.: Equation estimation of porosity and hydraulic conductivity of Ruhrtal aquifer
486 in Germany using near surface geophysics. *J. Appl. Geophys.*, 84, 77-85, doi:
487 10.1016/j.jappgeo.2012.06.001, 2012.

488 Proce, C., Ritzi, R. W., Dominic, D., and Dai, Z.: Modeling multiscale heterogeneity and aquifer
489 interconnectivity, *Ground Water*, 42, 658-670, 2004.

490 Ritzi R., Dai, Z., Dominic, D., Rubin Y.: Reply to comment by Shlomo P. Neuman on “Spatial correlation
491 of permeability in cross-stratified sediment with hierarchical architecture”. *Water Resour. Res.*, 42,
492 W05602, doi:10.1029/2005WR004402, 2006.

493 Ritzi R., Dai, Z., and Dominic, D.: Spatial correlation of permeability in cross-stratified sediment with
494 hierarchical architecture. *Water Resour. Res.*, 40, W03513, doi: 10.1029/2003wr002420, 2004.

495 Samper, F.J., and Neuman, S.P.: Adjoint state equations for advective-dispersive transport: Proceeding
496 of the 6th International Conference in Finite Elements in Water Resource, 423-437, New York, doi:
497 10.1007/978-3-662-11744-6_31, 1986.

498 Samper, J., Dai, Z., Molinero, J., García-Gutiérrez, M., Missana, T., and Mingarro, M.: Inverse modeling
499 of tracer experiments in FEBEX compacted Ca-bentonite. *Physics and Chemistry of the Earth*, 31, 640-
500 648, 2006.

501 Sikandar, P., Bakhsh, A., Arshad, M., and Rana, T.: The use of vertical electrical sounding resistivity
502 method for the location of low salinity groundwater for irrigation in Chaj and Rachna Doabs, *Environ.*
503 *Earth Sci.*, 60, 1113-1129, doi: 10.1007/s12665-009-0255-6, 2010.

504 Soltanian, M.R., Ritzi, R.W., Huang, C.C., and Dai, Z.: Relating reactive solute transport to hierarchical
505 and multiscale sedimentary architecture in a Lagrangian-based transport model: 2: Particle displacement
506 variance. *Water Resour. Res.*, 51, 1601-1618, doi: 10.1002/2014wr016354, 2015.

507 Soupios, P.M., Kouli, M., Vallianatos, F., Vafidis, A., and Stavroulakis, G.: Estimation of aquifer
508 hydraulic parameters from surficial geophysical methods: A case study of Keritis Basin in Chania (Crete-
509 Greece), *J. Hydrol.*, 338, 122-131, doi: 10.1016/j.jhydrol.2007.02.028, 2007.

510 Utom, A.U., Odoh, B.I., Egboka, B.C.E., Egboka, N.E., and Okeke, H.C.: Estimation of subsurface
511 hydrological parameters around Akwuke, Enugu, Nigeria using surface resistivity measurements. *J.*
512 *Geophys. Eng.*, 10, 025016, doi: 10.1088/1742-2132/10/2/025016, 2013.

513 Weissmann, G.S., and Fogg, G.E.: Multi-scale alluvial fan heterogeneity modeled with transition
514 probability geostatistics in a sequence stratigraphic framework. *J. Hydrol.*, 226, 48–65, doi:
515 10.1016/S0022-1694(99)00160-2, 1999.

516 Weissmann, G.S., S.F. Carle, G.E. Fogg, Three-dimensional hydrofacies modeling based on soil surveys
517 and transition probability geostatistics, *Water Resour. Res.*, 35(6), 1761–1770, 1999.

518 Weissmann, G.S., Yong, Z., Fogg, G.E., Blake, R.G., Noyes, C.D., and Maley, M.: Modeling alluvial fan
519 aquifer heterogeneity at multiple scales through stratigraphic assessment. Proceedings of the International
520 Groundwater Symposium: Bridging the gap between measurement and modeling in heterogeneous media,
521 Lawrence Berkeley National Laboratory, Berkeley, California, p25-28, 2002a.

522 Weissmann, G.S., Mount, J.F., and Fogg, G.E.: Glacially driven cycles in accumulation space and
523 sequence stratigraphy of a stream-dominated alluvial fan, San Joaquin Valley, California, USA, *J. of*
524 *Sediment. Res.* 72 (2), 240-251, 2002b.

525 Weissmann, G.S., Hartley, A.J., Nichols, G.J., Scuderi, L.A., Olson, M., Buehler, H., and Banteah, R.,
526 Fluvial form in modern continental sedimentary basins: the distributive fluvial system (DFS) paradigm:
527 *Geology*, 38, 39-42, doi: 10.1130/G30242.1, 2010.

528 Weissmann, G.S., Hartley, A.J., Scuderi, L.A., Nichols, G.J., Davidson, S.K., Owen, A., Atchley, S.C.,
529 Bhattacharyya, P., Chakraborty, T., Ghosh, P., Nordt, L.C., Michel, L., and Tabor, N.J., Prograding
530 distributive fluvial systems – geomorphic models and ancient examples, in Driese, S.G., and Nordt, L.C.
531 (eds), *New Frontiers in Paleopedology and Terrestrial Paleoclimatology*, SEPM Special Publication No.
532 104, p. 131-147, 2013.

533 Wu, Y., Guo, J., and Qiang, J.: Assessing the total dissolved solid in groundwater on basis of resistivity.
534 Conference on Groundwater Survey and Monitoring Technology, Baoding Hebei, China, 2003. (In
535 Chinese)

536 Yang, C., Dai, Z., Romanak, K., Hovorka, S., and Trevino, R.: Inverse Modeling of Water-Rock-CO₂
537 Batch Experiments: Implications for Potential Impacts on Groundwater Resources at Carbon
538 Sequestration Sites, *Environ. Sci. Technol.*, 48, 2798–2806, doi: 10.1021/es4041368, 2014.

539 Yang, Y., Luo, Y., Liu, M., Wang, R., and Wang, H.: Research of features related to land subsidence and
540 ground fissure disasters in the Beijing Plain: Prevention and Mitigation of Natural and Anthropogenic
541 Hazards due to Land Subsidence - Proc. IX Int. Symp. on Land Subsidence, K. Daito et al. eds., Proc.
542 IAHS,UK, 372, 239-242, 2015.

543 Yeh, T.C., Liu, S., Glass, R.J., Baker, K., Brainard, J.R., Alumbaugh, D., and LaBrecque, D.: A
544 geostatistically based inverse model for electrical resistivity surveys and its applications to vadose zone
545 hydrology. *Water Resour. Res.*, 38, 1278, doi: 10.1029/2001wr001204, 2002.

546 Zappa, G., Bersezio, R., Felletti, F., and Giudici, M.: Modeling heterogeneity of gravel-sand, braided
547 stream, alluvial aquifers at the facies scale. *J. Hydrol.*, 325,134-153, doi :10.1016/j.jhydrol.2005.10.016,
548 2006.

549 Zhu, L., Gong, H., Li, X., Li, Y., Su, X., and Guo, G.: Comprehensive analysis and artificial intelligent
550 simulation of land subsidence of Beijing, China. *Chin. Geogra. Sci.*, 23, 237–248, doi: 10.1007/s11769-
551 013-0589-6, 2013.

552 Zhu, L., Gong, H., Li, X., Wang, R., Chen, B., Dai, Z., and Teatini, P.: Land subsidence due to
553 groundwater withdrawal in the northern Beijing plain, China, *Eng. Geol.*, 193, 243-255, doi:
554 10.1016/j.enggeo.2015.04.020, 2015.

555 Zhu, L., Dai, Z., Gong, H., Gable, C., and Teatini, P.: Statistic inversion of multi-zone transition
556 probability models for aquifer characterization in alluvial fans. *Stoch. Environ. Res. Risk Assess.*, 30,
557 1005-1016, doi: 10.1007/s00477-015-1089-2, 2016a.

558 Zhu, L., Gong, H., Chen, Y., Li, X., Chang, X., and Cui, Y.: Improved estimation of hydraulic
559 conductivity by combining stochastically simulated hydrofacies with geophysical data. *Sci. Rep.*, 6, 22224,
560 doi: 10.1038/srep22224, 2016b.

561 **Table 1 Values of the volumetric proportion for the various facies in three zones**

Zone	Sub-clay and clay	Fine sand	Medium-coarse sand	Gravel
Zone 1	0.166	0.234	0.067	0.533
Zone 2	0.409	0.286	0.065	0.240
Zone3	0.503	0.328	0.106	0.063

568

569

570

571 **Table 2 Statistical data of logarithm hydraulic conductivity ($\log_{10}(m/d)$) in the three zones of the Chaobai**
 572 **alluvial fan**

Zone	Parameter	Fine sand	Medium-coarse sand	Gravel
	Mean	1.07	1.82	2.92
Zone 1	Minimum	-0.94	1.22	2.26
	Maximum	1.65	2.45	3.66
	Proportion	0.36	0.12	0.32
	Mean	0.42	1.17	2.65
Zone 2	Minimum	-2.22	-0.23	0.95
	Maximum	1.22	2.07	3.38
	Proportion	0.23	0.14	0.31
	Mean	0.17	0.81	2.48
Zone 3	Minimum	-2.64	-0.78	0.34
	Maximum	0.72	1.43	3.21
	Proportion	0.35	0.17	0.12

573

574

575

576

577
578

Table 3 Optimized parameters in the fitting exponential function of $\log_{10}(K)$ semivariogram in vertical direction for the various facies and zones

Zone	Parameter	Fine sand		Medium-coarse sand		Gravel	
		Estimated value	Confidence Interval (95%)	Estimated value	Confidence Interval (95%)	Estimated value	Confidence Interval (95%)
Zone 1	Variance	0.23	(0.19, 0.28)	0.32	(0.29, 0.34)	1.60	(1.41, 1. 81)
	Range (m)	6.01	(2.01, 20.52)	8.01	(1.53, 14.67)	6.50	(6.50, 12.84)
Zone 2	Variance	0.069	(0.067, 0.070)	0.14	(0.13, 0.15)	1.22	(1.19, 1.24)
	Range (m)	3.13	(1.83, 4.42)	8.27	(3.61, 12.93)	15.0	(12.33, 17.67)
Zone3	Variance	0.05	(0.047, 0.053)	0.126	(0.118, 0.135)	0.62	(0.54, 0.7)
	Range (m)	6.52	(2.19, 10.85)	2.72	(0.20, 6.55)	5.98	(0.20, 15.63)

579

580 **Table 4 Variances of $\log_{10}(K)$ of different facies along the dip direction in Zone 2 and Zone 3**

Zone		Fine sand	Medium-coarse sand	Gravel
Zone 2	Estimated value	0.10	0.15	1.38
	Confidence Interval (95%)	(0.059, 0.141)	(0.071, 0.228)	(1.14, 1.62)
Zone 3	Estimated value	0.045	0.068	0.48
	Confidence Interval (95%)	(0.030, 0.0607)	(0.043, 0.093)	(0.22, 0.73)

581

582 **Figure captions**

583 Figure 1 Chaobai alluvial fan in the north of Beijing Plain. (a) Location of the study area and distribution
584 of the field data. (b) Map of the hydraulic conductivity issued by Beijing Institute of Hydrogeology and
585 Engineering Geology (2007). The location of the study area is shown in the inset.

586 Figure 2 Flowchart of the geostatistical methodology

587 Figure 3 Typical depth behaviors of resistivity and corresponding stratigraphy in the eastern part of Zone
588 2

589 Figure 4 Inversed resistivity and corresponding stratigraphy in Zone 1

590 Figure 5 Histograms of $\log_{10}K$ for fine sand, medium-coarse sand and gravel

591 Figure 6 Experimental (circle symbol) and model (solid line) semivariogram along the vertical direction
592 for the various hydrofacies in the three zones. Notice that the range in the y-axis differs for gravel
593 lithology.

594 Figure 7 Experimental (circle symbol) and model (solid line) semivariogram along the dip direction for
595 the various hydrofacies in Zone 2 and Zone 3. Notice that the range in the y-axis differs for gravel
596 lithology.

597 Figure 8 Experimental (circle symbol) and model (solid line) composited semivariogram along the
598 vertical direction for the three zones.

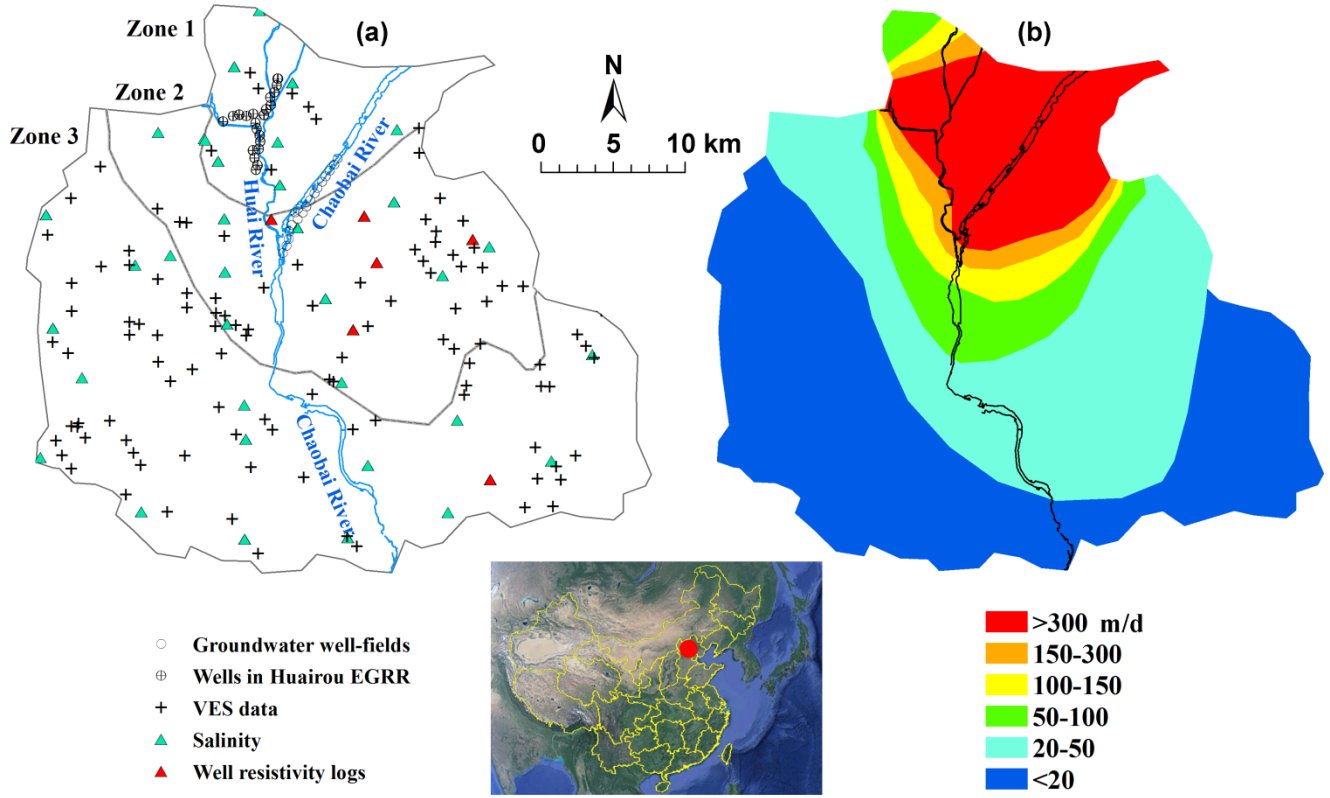
599 Figure 9 Distribution of hydrofacies (after Zhu et al., 2015a) and $\log_{10}(K)$ in the three-dimensional domain
600 representing the Chaobai alluvial fan: (a) axonometric projection of the three-dimensional system and (b)
601 vertical sections along the A-A', B-B', C-C' and D-D' alignments. The vertical exaggeration is 25. The
602 selected cell size is 300 m in north-south and east-west directions and 5 m in vertical direction, with a
603 total number of 747, 540 cells. The thickness of the simulated domain is 300 m.

604

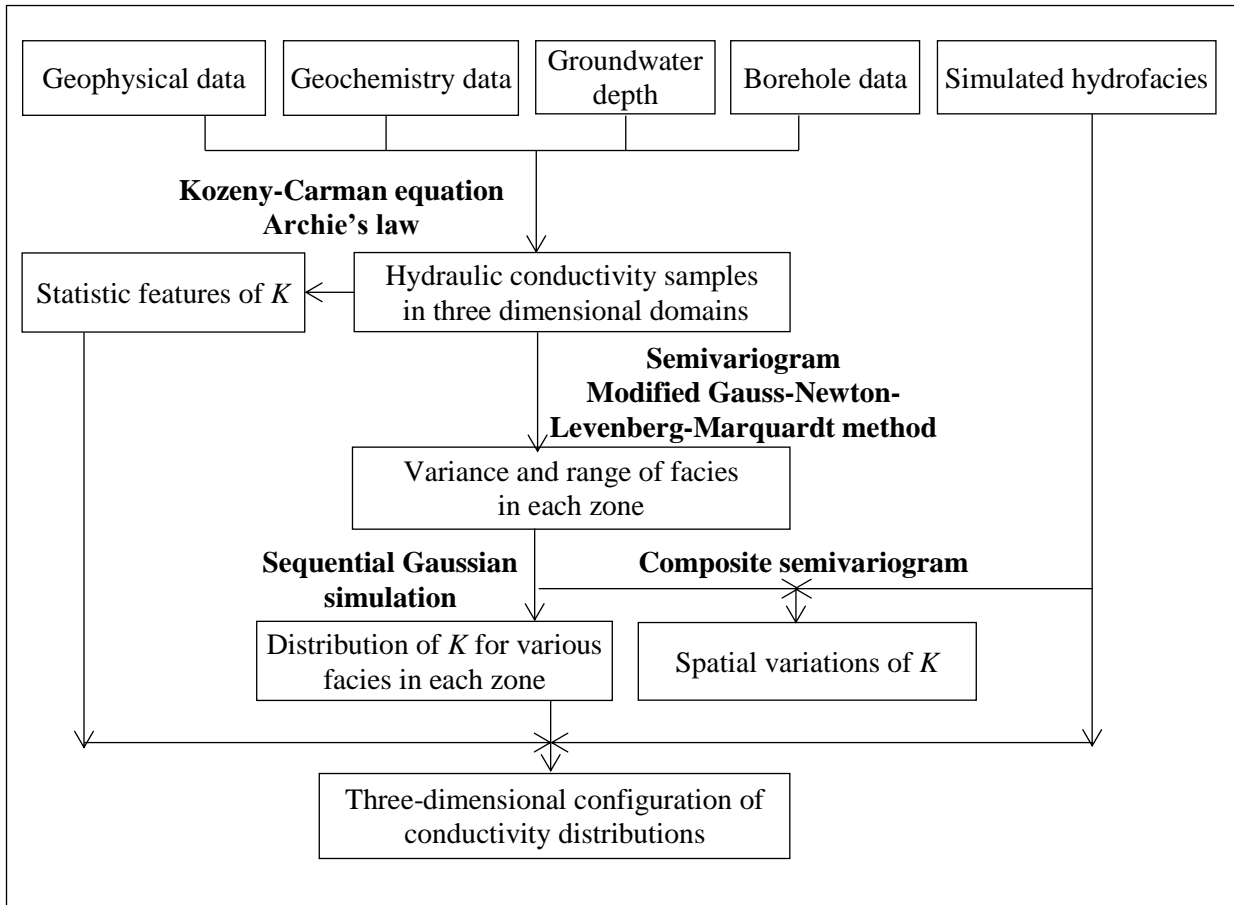
605

606

607



611



612

613

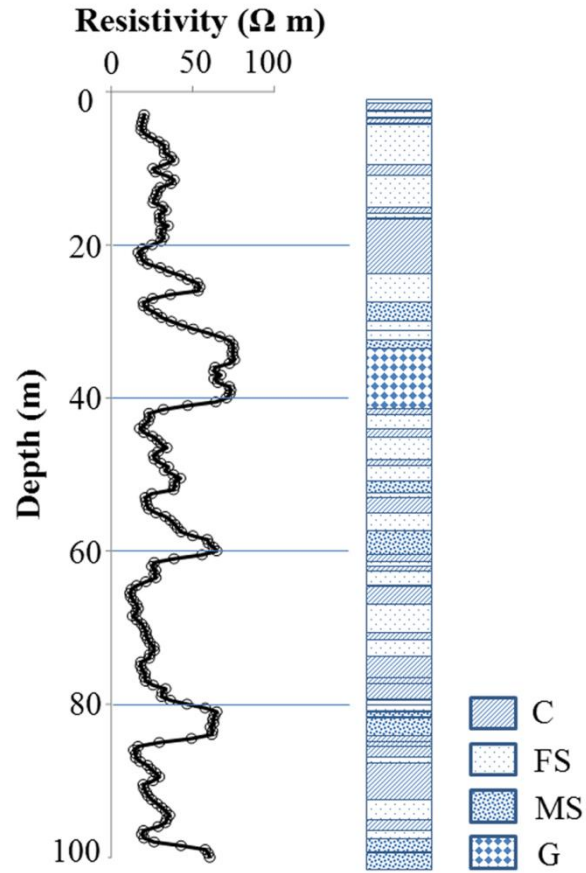
614

615

616

617 **Figure3**

618



619

620

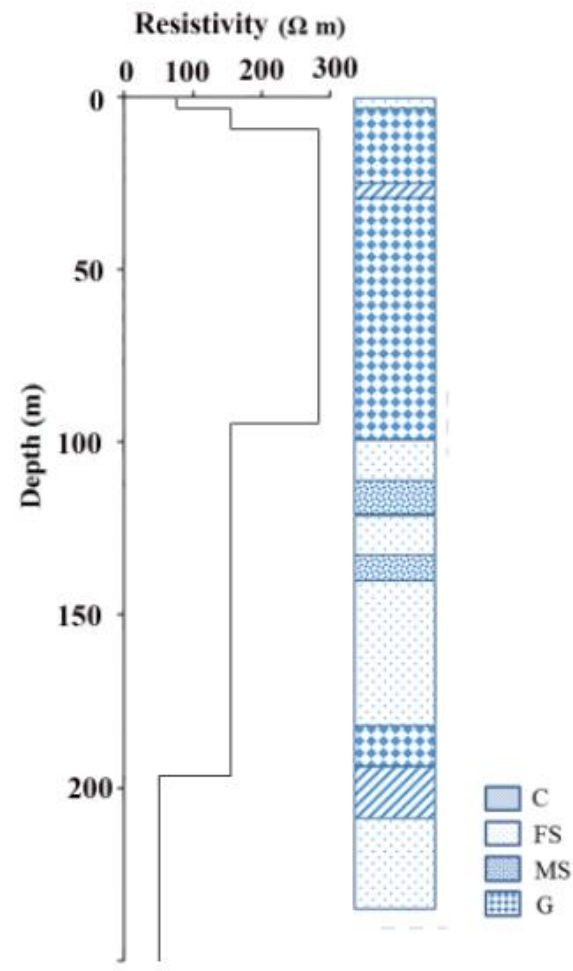
621

622

623

624

625 **Figure 4**



626

627

628

629

630

631

632

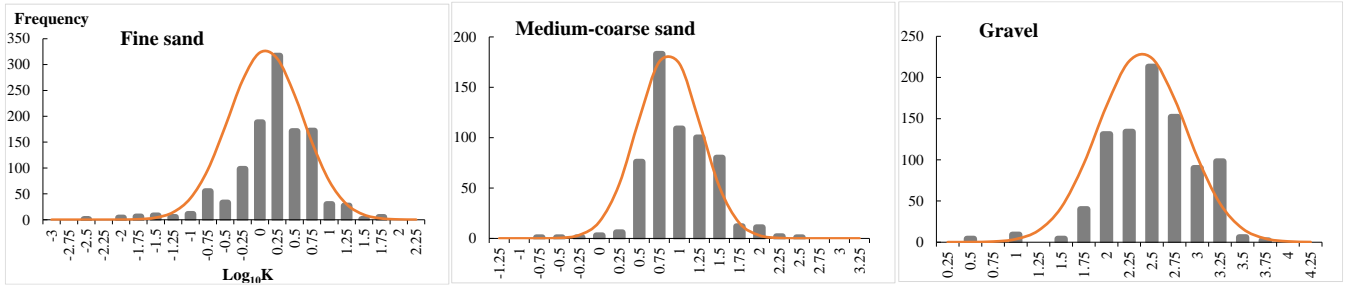
633

634

635

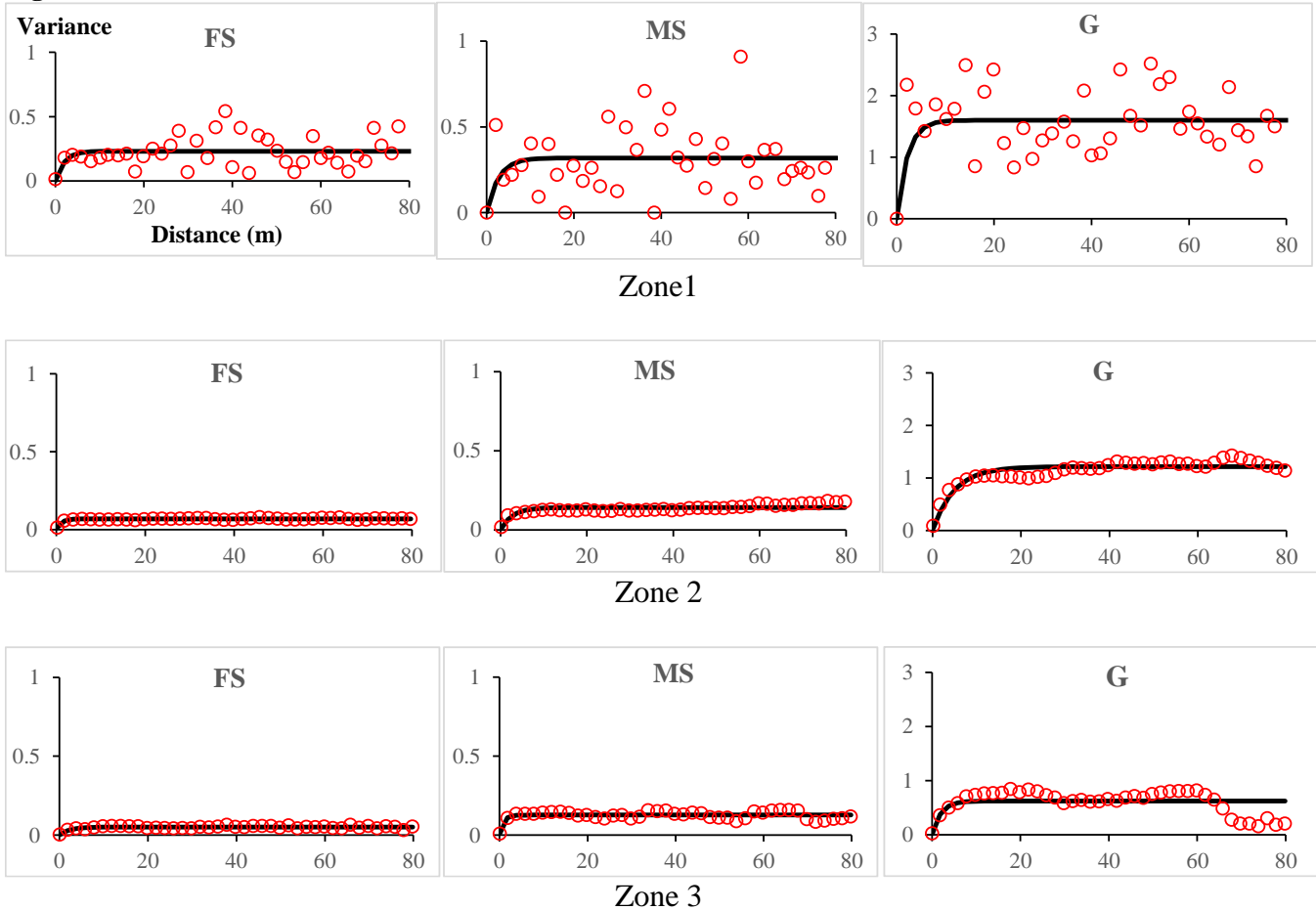
636
637
638

Figure 5



639
640
641
642

Figure 6

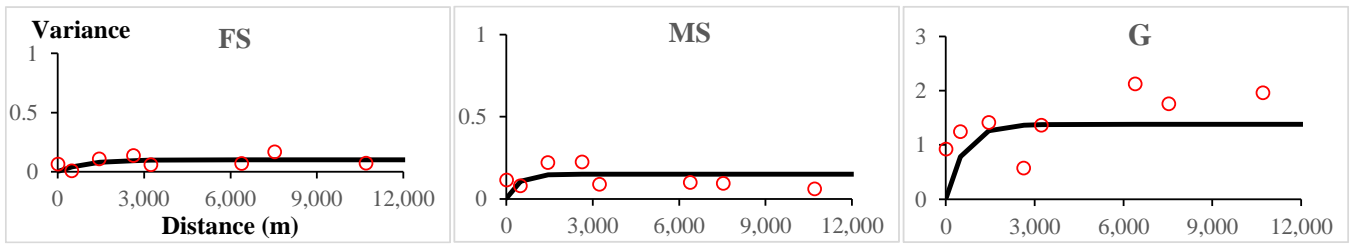


643
644
645

646
647
648

649
650

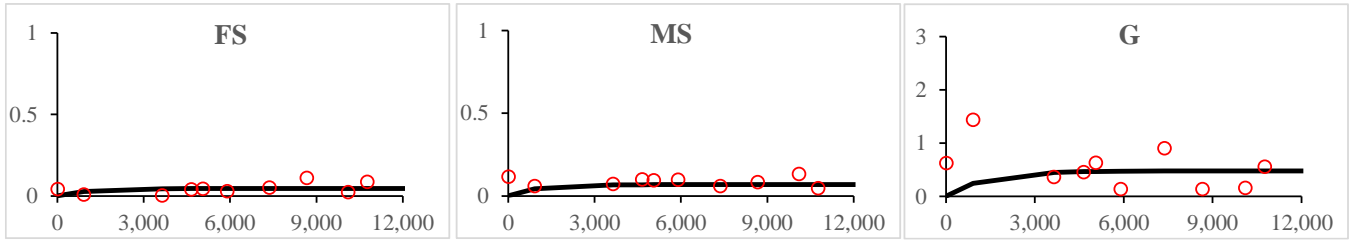
651 **Figure 7**



652

653

Zone 2



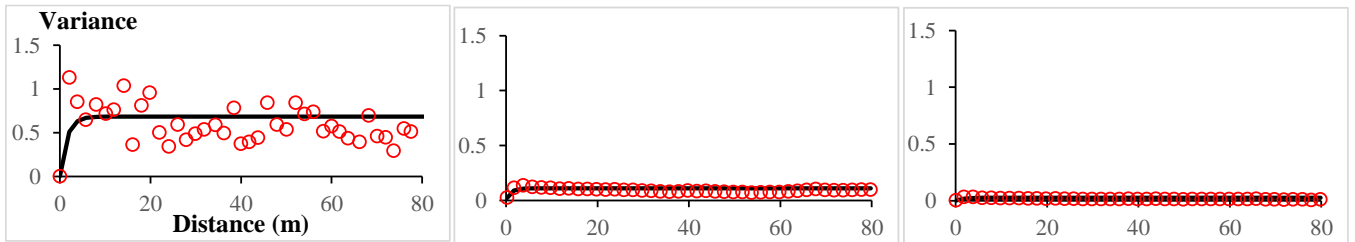
654

655

656

Zone 3

657 **Figure 8**



658

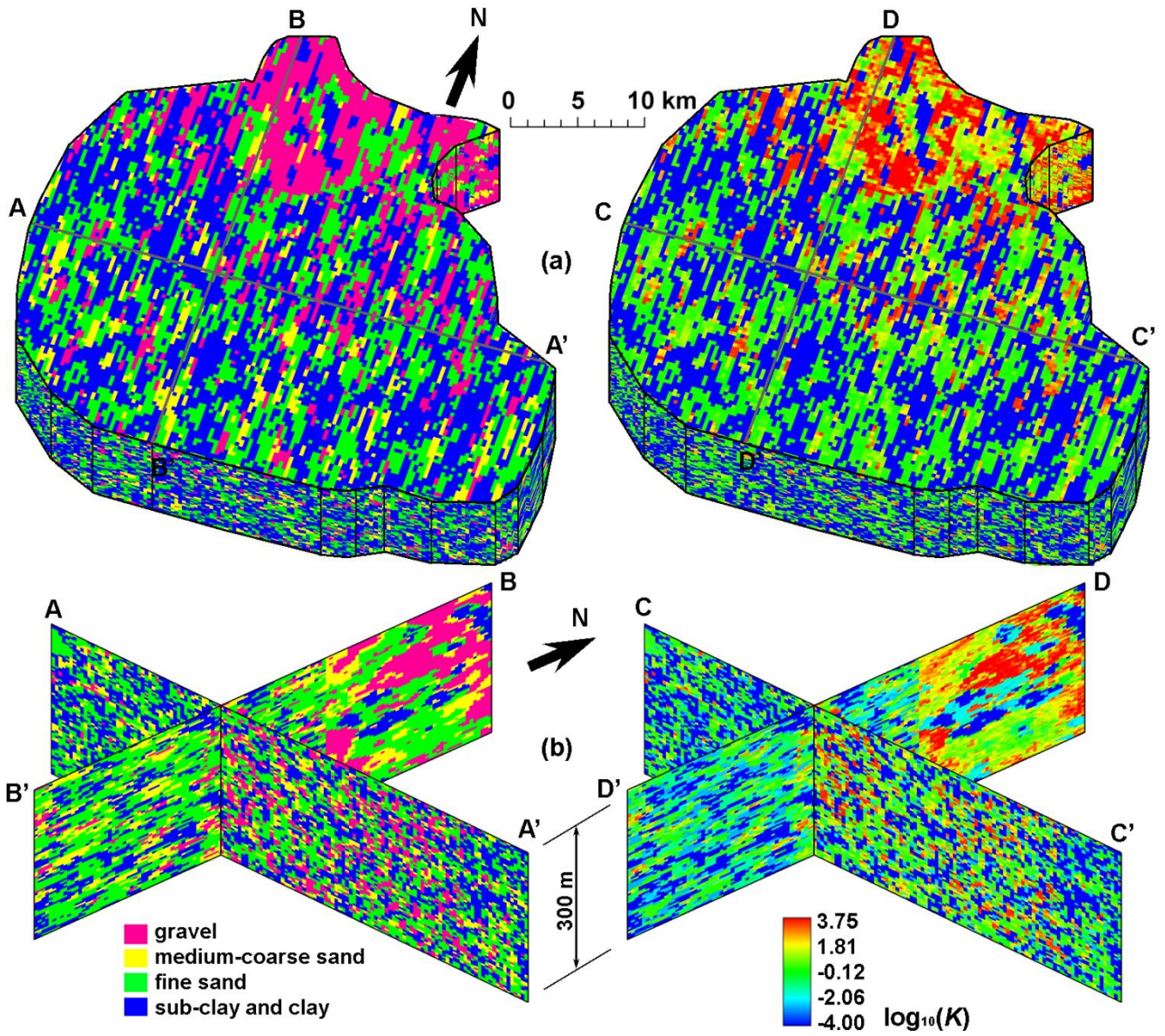
659

660

661

662

663



665

666

667